# Age-dating the Tully-Fisher relation at moderate redshift [*]

Ignacio Ferreras[1]†, Asmus Böhm[2], Bodo Ziegler[3], Joseph Silk[4]

[1] *Mullard Space Science Laboratory, University College London, Holmbury St Mary, Dorking, Surrey RH5 6NT*
[2] *Institute of Astro- and Particle Physics, Technikerstrasse 25/8, 6020 Innsbruck, Austria*
[3] *Department of Astrophysics, University of Vienna, Türkenschanzstr. 17, 1180, Wien, Austria*
[4] *Institut d'Astrophysique, Université Pierre et Marie Curie, 98 bis Boulevard Arago, 75014 Paris, France*

**ABSTRACT**
We analyse the Tully-Fisher relation at moderate redshift from the point of view of the underlying stellar populations, by comparing optical and NIR photometry with a phenomenological model that combines population synthesis with a simple prescription for chemical enrichment. The sample comprises 108 late-type galaxies extracted from the FORS Deep Field (FDF) and William Herschel Deep Field (WHDF) surveys at $z \lesssim 1$ (median redshift z=0.45). A strong correlation is found between stellar mass and the parameters that describe the star formation history, with massive galaxies forming their populations early ($z_{\rm FOR} \sim 3$), with star formation timescales, $\tau_1 \sim 4\,{\rm Gyr}$; although with very efficient chemical enrichment timescales ($\tau_2 \sim 1\,{\rm Gyr}$). In contrast, the stellar-to-dynamical mass ratio – which, in principle, would track the efficiency of feedback in the baryonic processes driving galaxy formation – does not correlate strongly with the model parameters. On the Tully-Fisher plane, no significant age segregation is found at fixed circular speed, whereas at fixed stellar-to-dynamical mass fraction, age splits the sample, with older galaxies having faster circular speeds at fixed $M_s/M_{\rm dyn}$. Although our model does not introduce any prior constraint on dust reddening, we obtain a strong correlation between colour excess and stellar mass.

**Key words:** galaxies: evolution – galaxies: formation – galaxies: stellar content – galaxies: fundamental parameters.

## 1 INTRODUCTION

Scaling relations among independent observational properties reveal the presence of important mechanisms underlying the formation and evolution of galaxies, and the interplay between the baryons and the dark matter halos where galaxies reside. The strong correlation between luminosity and circular speed in disc galaxies (i.e. the Tully-Fisher relation, Tully & Fisher 1977, hereafter TFR) has been used not only as an important rung in the cosmological distance ladder (e.g. Giovanelli et al. 1997), but also as a strong constraint on models of galaxy formation (e.g. Mathis et al. 2002; Dutton et al. 2007). Its highest correlated version – the baryonic TFR (McGaugh et al. 2000) – has even been used to test the validity of standard Newtonian mechanics (McGaugh 2012). The redshift evolution of the TFR allows us to constrain the star formation and assembly histories (see, e.g., Portinari & Sommer-Larsen 2007). From the observational side, there are technical challenges that make the interpretation of the velocity field and the determi-

nation of M/L ratios rather complicated. After the first results regarding the redshift evolution of the TFR (e.g. Vogt et al. 1996), a number of papers followed, claiming an evolution of the TFR slope (Ziegler et al. 2002; Böhm et al. 2004), with low-mass disks being more luminous in the the past. However, the analysis of Weiner et al. (2006) showed, instead, a significant brightnening of massive galaxies at high redshift, a result that could be reconciled if the star formation histories of massive galaxies have shorter timescales, as expected from multi-colour studies of disk galaxies (see, e.g., Ferreras et al. 2004). Constraining in a robust way the TFR is clearly a difficult task; the scatter of the relation is rather large for the amount of evolution observed, the outcome depends sensitively on the passband used, and samples at z∼1 are inherently biased towards the brightest galaxies (Fernández-Lorenzo et al. 2009). Furthermore, Böhm & Ziegler (2007) demonstrated that an evolution of the TFR scatter can mimic an evolution in slope. In addition, the complexity of disk kinematics is difficult to disentangle with single slit measurements, whereas 2D velocity fields from Integral Field Unit data suggest no evolution of slope, intercept or scatter of the TFR in disks with uniform kinematics, although the samples considered are rather small and also prone to biases (Flores et al. 2006; Puech et al. 2008).

Although semi-analytical models of galaxy formation predict a redshift evolution of the TFR in rough agreement with the ob-

---

servations, important pieces in the modelling of star formation are still missing (see, e.g. Tonini et al. 2011). In this paper, we apply a simple phenomenological approach to gain insight on the TFR from the point of view of the underlying stellar populations. The more physically motivated version of the TFR, namely the correlation between circular speed and stellar mass, is an important indicator of disk galaxy formation. Comparisons with evolution models allow us to use stellar mass instead of luminosity, reducing the highly variable changes in optical luminosity caused by the presence of young stars. The focus of this paper is to deconstruct the stellar mass TFR by exploring the age distribution of the stellar populations. In Ferreras et al. (2004) we already showed that the stellar ages of disk galaxies at moderate redshift were a strong function of galaxy mass, possibly explained by a significant change in the star formation efficiency, with a strong increase at a circular speed $V_{\mathrm{MAX}} > 140\,\mathrm{km\,s^{-1}}$. The mass-dependence of the stellar population properties of galaxies is a well-known phenomenon in the local universe (e.g. Kauffmann et al. 2003). Age indicators, like the strength of the 4000 Å break (Bruzual 1983), increase towards higher stellar masses, implying that high-mass galaxies formed stars with higher efficiency than low-mass ones in the cosmic past (Pérez-González et al. 2008). The connection between the mass of a galaxy and its stellar populations is also deeply intertwined with the evolution of the processes that drive galaxy formation over cosmic timescales. Overall, the main site of star formation shifts from high-mass galaxies at high redshift to successively lower-mass galaxies towards lower redshifts. This evolutionary trend is often referred to as downsizing (see, e.g. Cowie et al. 1996; Kodama et al. 2004; Cimatti et al. 2006). Several feedback processes have been proposed to explain such relationships, e.g. supernova feedback that regulates star formation in low-mass galaxies (e.g. Governato et al. 2009), or suppression of star formation by active galactic nuclei in the center of high-mass galaxies (e.g. Khalatyan et al. 2008). It is still an ongoing debate whether the governing factor in such correlations is the stellar mass of a galaxy or rather the mass of its host dark matter halo. In the latter case, environment rather than mass would actually be the key factor that shapes the stellar populations. However, studies based on very large samples from the Sloan Digital Sky Survey (e.g. van den Bosch et al. 2008; Rogers et al. 2010) present evidence that, at least at the present cosmic epoch, galaxy properties such as optical colour or morphological concentration are tightly correlated with stellar mass but only weakly with halo mass.

In this paper, we revisit the evolution of disk galaxies by studying a sample at moderate redshift (z∼0.5), with the aim of probing the evolution of the TFR and other scaling relations with respect to stellar ages. The outline of the paper is as follows: We present the photometric data from the FDF and WHDF samples (Section 2), and the phenomenological model to describe the star formation histories, including a comparison with more standard models of galactic chemical enrichment (Section 3), followed by a discussion of the main results (Section 4), along with our conclusions (Section 5). Throughout this paper, a standard ΛCDM cosmology is assumed, with $\Omega_m = 0.3$ and $H_0 = 70\,\mathrm{km\,s^{-1}Mpc^{-1}}$.

## 2   THE SAMPLE

A sample of field disc galaxies is selected from the multi-band imaging of the FORS Deep Field (FDF, Heidt et al. 2003) and William Herschel Deep Field (WHDF, Metcalfe et al. 2001) surveys. This sample was originally selected for the analysis of disc

kinematics in the redshift range $0.1 < z < 1.0$, using follow-up spectroscopic data taken with the FORS camera at the Very Large Telescope (see, e.g., Böhm et al. 2004; Böhm & Ziegler 2007). In multi-object spectroscopy mode, a slit was placed along the apparent major axis of each target to extract a rotation curve, i.e. the rotation velocity as a function of radius. *Hubble Space Telescope* imaging with the Advanced Camera for Surveys (ACS) was used to determine parameters such as position angle, disc inclination or scale length, with the use of the GALFIT package (Peng et al. 2002). Taking into account all geometrical effects, such as inclination, and all observational effects, such as seeing and slit width, the intrinsic maximum rotation velocity $V_{\mathrm{MAX}}$ was determined for all galaxies with regular rotation curves. Neglecting objects with disturbed kinematics, solid-body rotation or a too low signal-to-noise ratio to probe into the regime of constant rotation velocity at large radii, $V_{\mathrm{MAX}}$ could be determined for 124 galaxies, with a median uncertainty of $\Delta \log V_{\mathrm{MAX}} = 0.087$ dex.

Photometry of our sample is available from the FDF and WHDF survey data. The FDF photometry has been acquired with the Very Large Telescope in the $U$-, $B$-, $g$-, $R$- and $I$-bands, and the New Technology Telescope in the $J$- and $K_s$-bands. The WHDF photometry was carried out at the William Herschel Telescope in the $U$-, $B$-, $R$-, and $I$-bands and the Calar Alto 3.5m telescope in the $H$- and $K$-bands. Fixed aperture photometry was performed after convolving all frames to a common PSF with FWHM 1 (1.5) arcsec for FDF (WHDF) galaxies. The aperture diameter used for the photometry is 2 (3) arcsec for FDF (WHDF) sources. The final magnitudes were corrected for Galactic extinction following Cardelli et al. (1989), adopting a reddening $E(B - V) = 0.018$ mag and $E(B - V) = 0.030$ mag towards the positions of the FDF and WHDF, respectively (based on Schlegel et al. 1998). A number of galaxies with available $V_{\mathrm{MAX}}$ values were not observed in all filters and thus rejected, resulting in a final sample of 108 disks (73 in FDF and 35 in WHDF), between $z = 0.07$ and $z = 0.97$ at a median redshift of $\langle z \rangle = 0.45$.

Star formation rates (SFRs) were estimated from [O II] equivalent widths, available for 65 galaxies, following Kennicutt (1992) (other emission lines, such as Hβ or [O III] are sometimes used for the determination of the rotation curves, depending on the wavelength range probed by a given spectrum). Note that Hα is not available within the observed wavelength range to derive SFRs given the redshift distribution of the sample.

Figure 1 shows a comparison of some of the available colours with respect to two sets of synthetic models from Bruzual & Charlot (2003): simple stellar populations (i.e. single age and metallicity, *left*) or composite models with an exponentially decaying star formation history, at fixed metallicity (i.e. $\tau$-models, *right*). Different lines correspond to choices of stellar age in SSP models (given by the formation redshift), or exponential timescale and metallicity for the $\tau$ models, as labelled. The combination of colours across a wide range of wavelengths allows us to constrain the ages and metallicities: the optical colours (*top*) are most sensitive to age, whereas the NIR colours have an increased dependence with respect to metallicity. All these models are dustless, except for the thin solid line in the $\tau$ models, which corresponds to an intrinsic reddening $E(B - V) = 0.2$ (following the Cardelli et al. 1989, extinction law). The comparison shows that the reddening values stay below $E(B - V) \lesssim 0.5$ mag. The figure also illustrates the need to choose composite models to explain the multi-band photometric data, as expected from the complex star formation histories of disc galaxies.
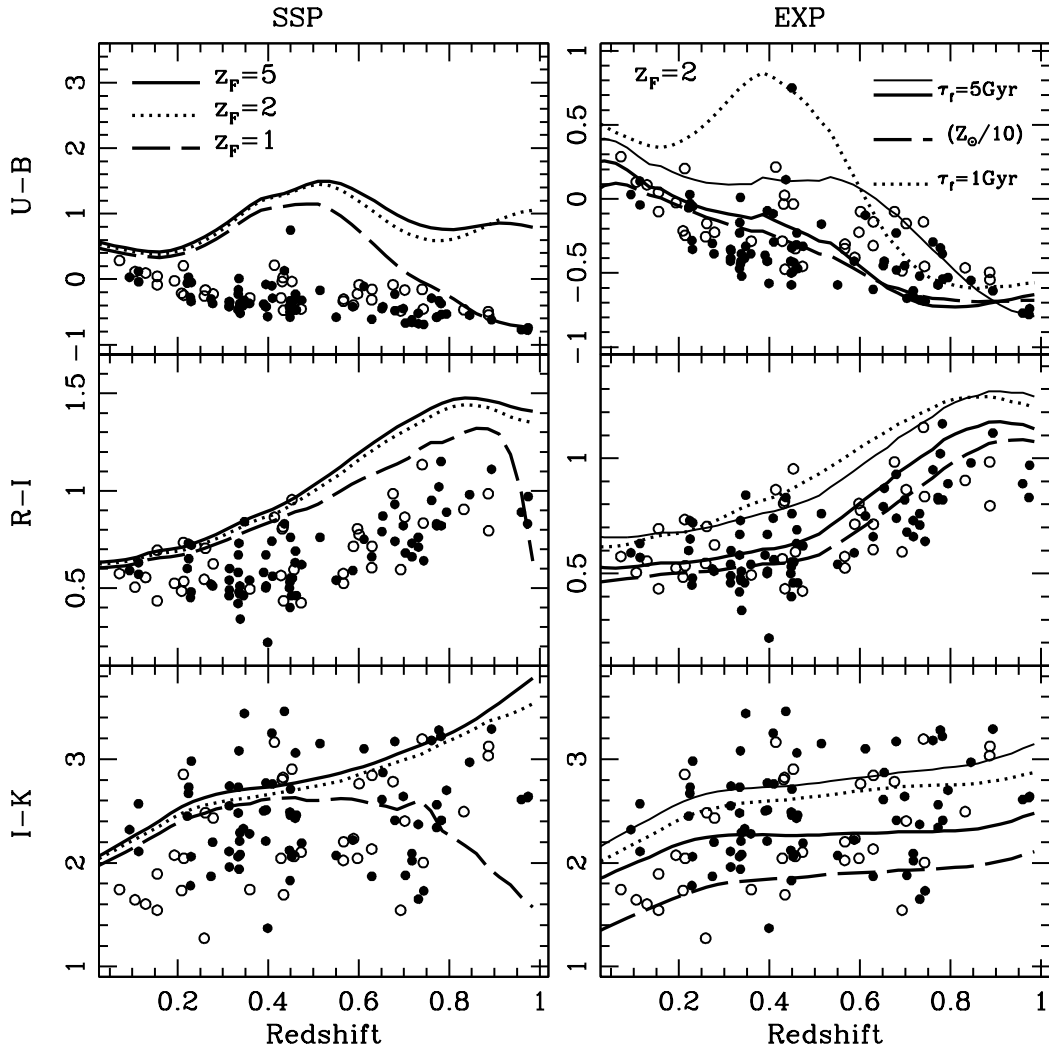
**Figure 1.** Comparison of the photometry with simple stellar populations (*left*) and models with exponentially decaying star formation histories at fixed metallicity (*right*), all based on the Bruzual & Charlot (2003) population synthesis models. The thin solid line in the EXP panels corresponds to a colour excess of $E(B - V) = 0.2$ mag for a $\tau_f = 5$ Gyr model, at solar metallicity. Galaxies in the FDF (WHDF) are shown as solid (open) dots, where a small offset (always below 0.1 mag) is applied to the WHDF data to correct for the different response of the filters used (only for display purposes in this figure).

## 3  MODELLING STAR FORMATION HISTORIES

We apply a phenomenological one-zone model that describes the star formation history (SFH) and chemical enrichment of a galaxy with three parameters. The model is constrained by the broadband photometric data presented above. A simple model allows us to probe a large volume of parameter space, deriving more consistent constraints on the mechanisms contributing to the build-up of the stellar populations. The star formation history is assumed to start at an epoch given by a formation redshift ($z_{\rm FOR}$), with a star formation rate modelled either by a delayed exponential:

$$\psi(t) \propto [t - t(z_{\rm FOR})]e^{-[t-t(z_{\rm FOR})]/\tau_1}, \qquad (1)$$

or by a standard exponential (i.e. a $\tau$-model):

$$\psi(t) \propto e^{-[t-t(z_{\rm FOR})]/\tau_1}, \qquad (2)$$

and a metallicity trend driven by the growth in stellar mass, although with an independent timescale, to take into account the effects of both gas outflows and star formation efficiency:

$$Z(t) \equiv Z_1 + Z_2\Big[1 - \exp^{-[t-t(z_{\rm FOR})]/\tau_2}\Big]. \qquad (3)$$

The extrema in metallicity are $Z_1 = Z_\odot/10$ and $Z_2 = 2Z_\odot$. In this model, $\tau_1$ gives an indication of the timescale for the formation of the stellar component, whereas $\tau_2$ drives the metal enrichment. These two timescales are considered independent parameters in the analysis, hence we allow for scenarios with a decoupling between star formation, gas infall and outflows. As an example, Fig. 2 shows the relationship between star formation rate (assuming a delayed exponential law) and metallicity for three models. Note that the dotted line, corresponding to a balance between enrichment and infall, gives a metallicity distribution similar to the closed box model, producing an excess of stars at low metallicity. This so-called G-dwarf
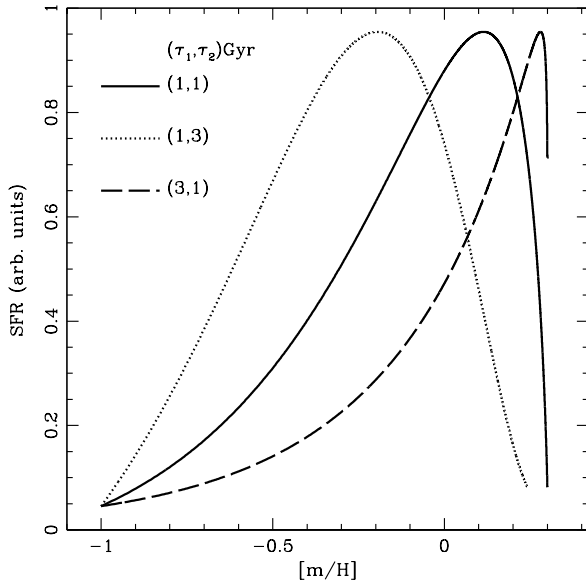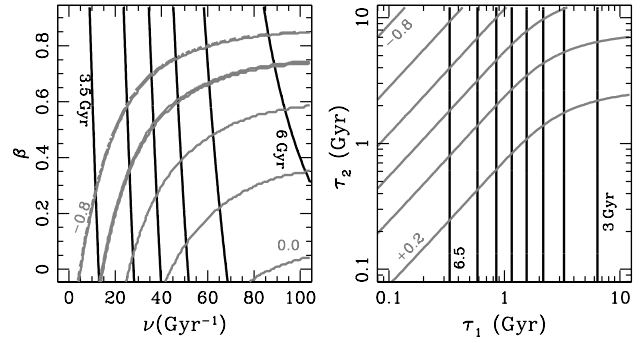
**Figure 2.** The model adopted to track the star formation histories of disc galaxies includes two different timescales: $\tau_1$ tracks the star formation rate – which evolves as a delayed exponential. $\tau_2$ controls the enrichment rate. This figure shows the difference in the time evolution of the star formation rate and the metallicity ([m/H]) for three cases, as labelled. An additional parameter (formation redshift) controls the average age of the distribution.



**Figure 3.** Comparison of the model used in this paper with a more generic chemical enrichment model that includes parameters to describe the star formation efficiency ($\nu$) and the fraction of gas ejected in outflows ($\beta$) (see e.g. Ferreras & Silk 2001, for details). In order to simplify the comparison, we assume the same formation epoch in both cases ($z_{\rm FOR} = 5$). The panel on the left shows contours of mass-weighted average age (black) and metallicity (grey), with respect to star formation efficiency and gas outflow fraction. The black (grey) labels indicate the extrema in age (metallicity). The panel on the right shows similar contours for the model used here, exploring a range of values of star formation timescale ($\tau_1$) and enrichment timescale ($\tau_2$).

problem (see, e.g., Pagel 1997) – is solved in this framework by a fast enrichment (short $\tau_2$) along with an extended period of infall (long $\tau_1$). In Fig. 3, we compare the age and metallicity distributions given by this model with a more detailed analysis based on standard prescriptions of chemical enrichment (see Ferreras & Silk 2001; Ferreras et al. 2004, for details). Contours of average stellar age (black lines) and metallicity (grey lines) are shown with respect to star formation efficiency ($\nu$) and outflow fraction ($\beta$) for the enrichment model (*left*) or with respect to the two timescales ($\tau_1$ and $\tau_2$) for the phenomenological model used here (*right*). The formation epoch is fixed in both cases to $z_{\rm FOR} = 5$. A mapping can be established between star formation efficiency ($\nu$) and our $\tau_1$; and also between outflow fraction ($\beta$) and our $\tau_2$. We emphasize that the model presented here is not only simpler, but it also gives a clearer description of the formation of the stellar populations.

## 4 RESULTS

The models presented in the previous section are explored over a large range of parameters. We also include the effects of dust as a homogeneous screen. We describe this component as an additional fourth free parameter, choosing the colour excess, $E(B{-}V)$, from the Cardelli et al. (1989) extinction law. In order to obtain the most robust estimates of the best fit *and uncertainty*, we opt for a comprehensive search of parameter space. This is doable given the small number of parameters describing the star formation history. Furthermore, a parameter search algorithm has a very simple parallelisation scheme, so that we can run it efficiently on many processors. For a choice of the four parameters, the resulting star formation history is combined with the synthetic populations of Bruzual & Charlot (2003) to derive the six (five) broadband pho-

tometric colours available from the FDF (WHDF) data, generating a likelihood (via a standard $\chi^2$ statistic), that defines a probability distribution function for the three parameters under consideration. Out of the two families of models – corresponding to either a delayed exponential, or a $\tau$ model – we select for each galaxy the one that gives the lowest value of the $\chi^2$. Although discriminating between these two prescriptions for the star formation history is beyond the capabilities of broadband photometry, we note that there is a slight preference towards the delayed exponential model, especially at low stellar mass. We derive from this likelihood the average mass-weighted age and metallicity, along with the uncertainties, quoted throughout this paper at the 69% level. For each galaxy, we run two grids of $32^3 \times 16$ models (one for each choice of star formation rate), uniformly scaled over the following range of the parameters:

$$1 \leqslant z_{\rm FOR} \leqslant 5$$
$$-1 \leqslant \log(\tau_1/{\rm Gyr}) \leqslant +1$$
$$-1 \leqslant \log(\tau_2/{\rm Gyr}) \leqslant +1$$
$$0 \leqslant E(B-V) \leqslant 0.5$$

In addition, we impose a prior on the average stellar metallicity, using the local mass-metallicity relation of Gallazzi et al. (2005). We note that this prior is rather mild, given the large scatter of the distribution at fixed mass ($\Delta[Z/H] \sim 1$ dex at $\log M_s/M_\odot = 10$). The reason for imposing this prior is based on the lack of a large number of independent metallicities in the synthetic models, along with the fact that broadband photometry alone – only extending out to rest-frame data in the $H$ band, given the redshift range – cannot impose strong constraints on the metallicities of unresolved stellar populations. This prior helps to ensure a correct age-metallicity discrimination in the analysis. The error bars on the estimates of stellar metallicity are around $\Delta[Z/H] \sim 0.3$ dex and the average age uncertainties $\Delta\langle{\rm Age}\rangle/\langle{\rm Age}\rangle = 0.4$. A comparison between the ages derived with and without the prior on metallicity gives a difference $\langle{\rm Age}\rangle_{\rm PRIOR} - \langle{\rm Age}\rangle_{\rm NO\ PRIOR} =$
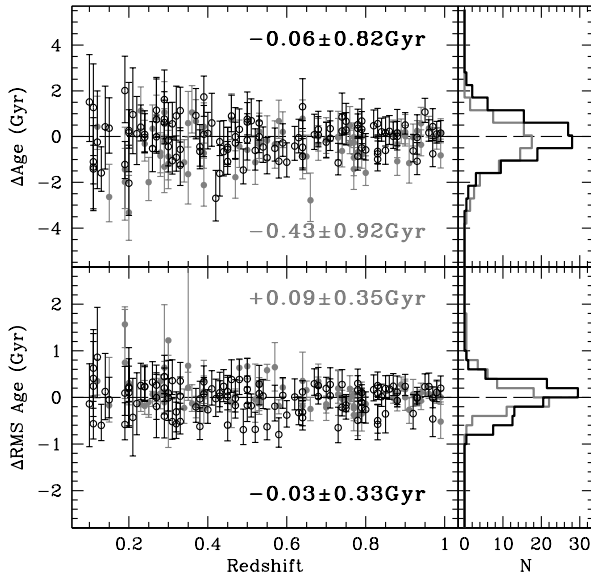
**Figure 4.** Recovery of average (top) and RMS of the age distribution (bottom) from 200 simulations spanning a similar range of redshift and SNR as the original data. The vertical axis in each panel represents input minus recovered value. The black (grey) data points use the metallicity prior from the Gallazzi et al. (2005) relation, assuming a stellar mass of $10^{11}\,M_\odot$ ($10^9\,M_\odot$). Error bars are the 69 % confidence levels from the analysis, and the histogram of the distribution is shown in the rightmost panels. The values of the difference in average age and RMS of each case is indicated with the same colour coding.
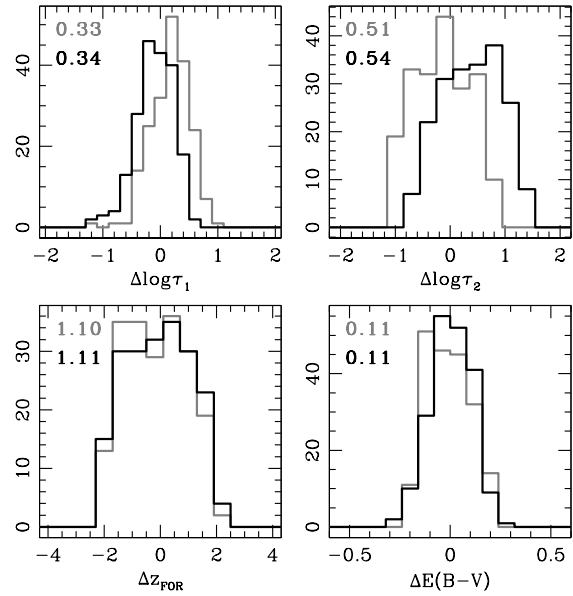


**Figure 5.** Recovery of model parameters from 200 simulations spanning a similar range of redshift and SNR as the original data. In each case $\Delta$ is defined as the difference between the input and the recovered parameter. The black (grey) histograms correspond to the application of the prior regarding the mass-metallicity relationship of Gallazzi et al. (2005) assuming galaxies with stellar mass of $10^9\,M_\odot$ ($10^{11}\,M_\odot$), to illustrate the effect of such a prior on the recovery of the model parameters (see text for details). The numbers in each panel show the RMS of the distributions for each choice of stellar mass, with the same colour coding.

$0.14 \pm 0.61\,$Gyr, without any systematic effect with respect to galaxy mass.

In order to confirm this point, we performed 200 simulations with the same redshift and signal-to-noise distribution as the original data, comparing the age and RMS of the age distribution. Fig. 4 shows the difference between the input and the recovered values for the average age (*top*) and the RMS of the age distribution (*bottom*). The simulations assume two different cases of stellar mass for the application of the prior: $10^{10}\,M_\odot$ (black) and $10^9\,M_\odot$ (grey). In either case, the recovered values do not show any systematic offset, with an accuracy of $\sim 0.9\,$Gyr in average age and $\sim 0.3\,$Gyr in the RMS of the age distribution. In Fig. 5 a similar comparison is made, in this case between the model parameters. The numbers in each panel give the RMS of the distributions of the (input − output) values of the parameters for the simulations. Note that there is no systematic change in the values of the parameters, except for $\tau_2$. In this case, as expected, the prior biases the values of metallicity towards lower metallicity for the $10^9\,M_\odot$ (grey) case, and towards higher metallicity at $10^{11}\,M_\odot$ (black) [1].
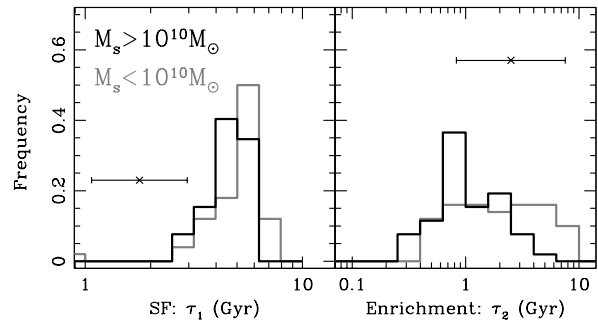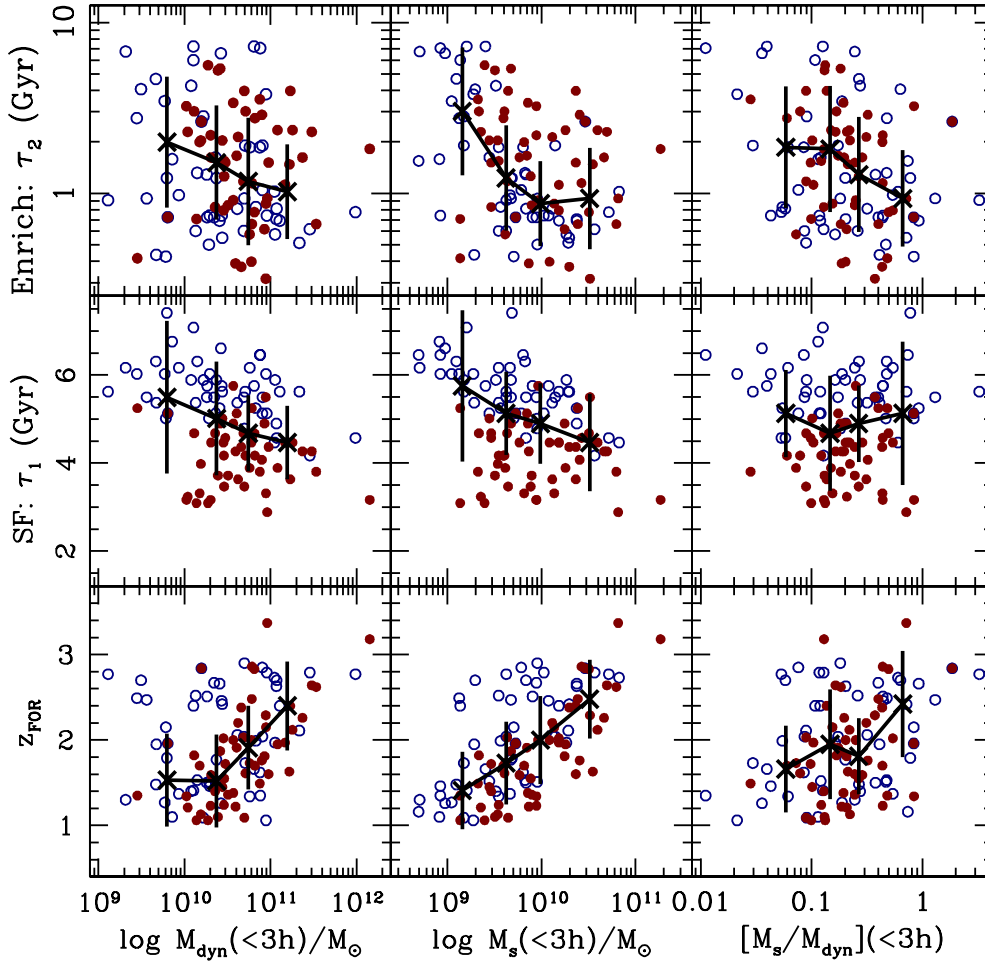
## 4.1 Model parameters

Hereafter, we present the results for the FDF/WHDF data. Fig. 6 shows the distribution of the two formation timescales. The sample



**Figure 6.** The model timescales $\tau_1$ (star formation) and $\tau_2$ (enrichment) are shown for our sample of FDF+WHDF disc galaxies, split with respect to stellar mass, as labelled. A typical $1\,\sigma$ error bar is shown.

is split with respect to stellar mass, at the position of the median ($\sim 10^{10}\,M_\odot$). For reference, the median uncertainty (at the 68% level) is shown in each panel as a horizontal error bar. Note the difference between the distribution of low- and high-mass discs, especially in the enrichment timescale, $\tau_2$. The majority of low-mass discs (grey histograms) are fitted by longer timescales both in star formation ($\tau_1$) and enrichment ($\tau_2$). A significant fraction of the massive galaxies are better explained by very short enrichment timescales ($\tau_2 \sim 1\,$Gyr). Low values of *both* $\tau_1$ and $\tau_2$ would represent the efficient and fast buildup of the stellar populations expected in early-type galaxies (see, e.g., de la Rosa et al. 2011). In contrast,

---

[1] We note that the prior for the simulations is blindly applied in all galaxies, irrespective of their input value of metallicity, hence representing a worst case scenario.

**Figure 7.** The constraints on the parameters of the models are shown as a function of total mass (*left*), stellar mass (*centre*) and stellar-to-total mass fraction (*right*). Individual values are shown as dots, whereas the black crosses represent the median values after binning (with equal number of galaxies per bin), including the RMS scatter per bin as an error bar. The red solid (blue open) dots correspond to $z \geqslant 0.45$ ($< 0.45$) (i.e. split at the median redshift of the sample).

massive discs have more extended star formation timescales (reflecting a lower star formation efficiency or an extended infall), and short enrichment timescales (possibly caused by a lack of metal-rich outflows). The difference in the error bars for $\tau_1$ and $\tau_2$ is caused by the higher accuracy on the age estimates, with respect to metallicity.

Fig. 7 shows the best fit parameters as a function of physical properties: dynamical mass (*left*), stellar mass (*centre*), or stellar-to-dynamical mass fraction (*right*). To avoid model-dependent extrapolations for the dark matter distribution, both dynamical and stellar masses are quoted within a fixed aperture of 3 exponential scale lengths (roughly where all galaxies in the sample reach a flat circular velocity). The scale lengths are derived from surface brightness fits to the ACS images (Böhm & Ziegler 2007). For a clearer interpretation of the trends, the individual data points are arranged into four bins. The binning is done at constant number of galaxies per bin, and the median and dispersion (RMS) are shown as crosses, and error bars, respectively. The individual data points are also coded with respect to redshift (red solid: $z \geqslant 0.45$; open

blue: $z < 0.45$). Note that the parameters are correlated with stellar mass, with a clear downsizing trend with $z_{FOR}$. The correlations with respect to $M_s/M_{dyn}$ could be explained with the assumption that this fraction is an indicator of efficiency or gas outflows, hence, at large stellar masses, one should expect a fast, efficient buildup of metallicity (i.e. a short $\tau_2$). Although such trend is present in the data, its correlation is much weaker than with respect to stellar mass. Regarding redshift, the strongest trend is with star formation/infall timescale ($\tau_1$, middle panels), reflecting a more extended distribution of ages in the sample at low redshift, mostly due to the wider range of ages because of lookback time.

The trends of average age and metallicity with stellar mass are shown in Fig. 8, split into three redshift bins, that correspond to uniform steps of $\sim 2$ Gyr in lookback times between bins. Error bars are shown at the 68% confidence level. A linear fit between age and mass is applied to the high redshift bin (top left panel), and shifted by the lookback time in the other two bins, for reference. Within error bars, the slopes are consistent, with the only change being an offset amounting to the change in lookback time. Although this
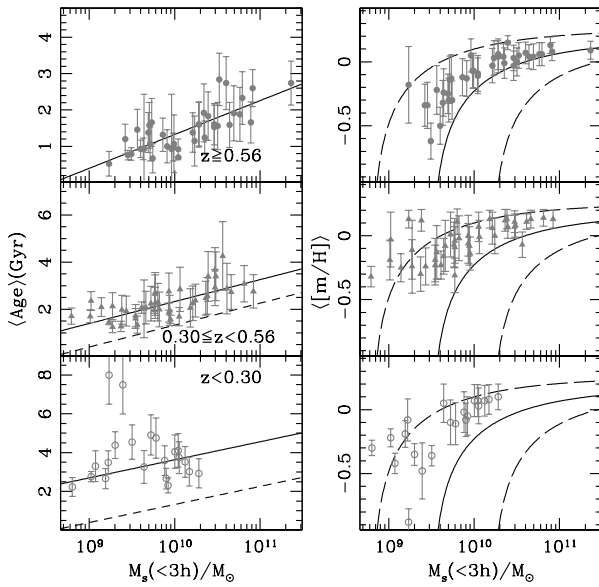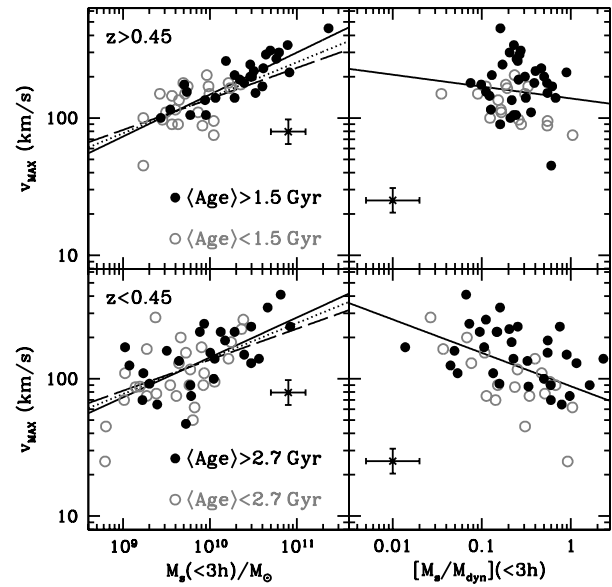
**Figure 8.** Distribution of ages (*left*) and metallicities (*right*) of the FDF+WHDF disc galaxies, split with respect to redshift in three panels. The straight line on the top-left panel fits the data points in the high red-shift subsample. This line is copied over, as a dashed line, in the other two redshift bins (middle- and bottom-left panels). We also show the effect of shifting this fit by the lookback time difference, as solid lines in these two panels. On the right, the solid and dashed lines mark the average and $1\sigma$ uncertainties of the mass-metallicity relation of Gallazzi et al. (2005) .



**Figure 9.** Relationship between maximum rotation velocity and stellar mass (*left*) or stellar-to-dynamical mass fraction (*right*). The sample is split at the median with respect to stellar average age. Top and bottom panels show subsamples at high and low redshift, respectively (also split at the median of the distribution). The solid line in each panel is the best fit to the data within each redshift bin. Typical error bars are shown. The dashed line in the left panels show the local relationship from the $I$-band determined stellar masses (Bell & de Jong 2001). The dotted line is the z~1 relationship from (Miller et al. 2012).

could be interpreted as a lack of "dynamical downsizing", the sample is not large enough to constrain a change in slope of the correlation between age and stellar mass. As regards to metallicity, there is a trend towards the metal rich envelope of the local mass-metallicity relation. Note the present analysis, based on broadband photometry alone, mainly constrains stellar ages, whereas estimates of metallicity carry a large error bar (typically $\Delta[Z/H] \sim 0.3$ dex). Even though the local mass-metallicity relation is used as a mild prior in the analysis, we stress that the minimum values of $\chi^2$ are not significantly affected by the prior, with $\sim 90\%$ of the sample having a reduced value $\chi_r^2 \lesssim 2$.

### 4.2 The evolution of the Tully-Fisher relation

Fig. 9 shows the properties of the underlying stellar populations on a variation of the Tully-Fisher diagram (Tully & Fisher 1977). The sample is split at the median redshift (top/bottom panels), and in each panel, black solid (grey open) circles represent disc galaxies with an average age older (younger) than the mean value within each redshift bin, as labelled. Typical ($1\sigma$) error bars are shown as reference. The panels on the left show a $V_{MAX}$ vs stellar mass Tully-Fisher relation. The usual downsizing relation between stellar mass and age is found. However, at fixed stellar mass, no significant segregation with respect to $V_{MAX}$ is evident. Old and young discs show a similar amount of scatter with respect to the best linear fit (solid line). The slope and intercept are indistinguishable (as also found by, e.g. Miller et al. 2011, 2012, out to z~1.7) with respect to the redshift subsample chosen ($M_s \propto V_{MAX}^{3.0}$). The panels on the right show the maximum circular speed with respect to stellar-to-dynamical mass fraction, with a clear trend towards

a faster $V_{MAX}$ for disc galaxies with a lower stellar mass fraction, as expected, since the stellar-to-total mass ratio decreases with increasing galaxy mass (see, e.g., Moster et al. 2010). At fixed mass fraction, the younger galaxies have slower rotation speeds. One can assume that the stellar-to-dynamical mass fraction controls the level of "baryon feedback" – mainly related to star formation in this sample. A tentative interpretation of the segregation with respect to age, at fixed $M_s/M_{dyn}$, would be that older galaxies are preferentially assembled in higher density haloes, therefore having a higher circular speed.

### 4.3 The contribution of dust

Fig. 10 shows the trend of dust reddening with respect to stellar mass, average metallicity or inclination. The sample is split at the median value of the stellar mass ($\sim 10^{10}$ M$_\odot$), with the red solid (blue open) dots corresponding to stellar masses above (below) this cut. The big solid dots with error bars in the left and middle panels give the median and RMS scatter of the complete sample, binned at fixed number of galaxies per bin. A prescription from Tully & Fouqué (1985) is included for reference, with $f = 0.2$ and $\tau = 0.5$ (solid line). A strong trend is found with respect to mass and metallicity, in good agreement with the observations of local disks (Tully et al. 1998). More subtle is the excess of more attenuated galaxies at higher inclinations for the more massive galaxies. Notice that our modelling does not impose any prior constraint on the colour excess, considering all values of $E(B-V)$ in the analysis. The formalism of Tully & Fouqué (1985) is applicable for the
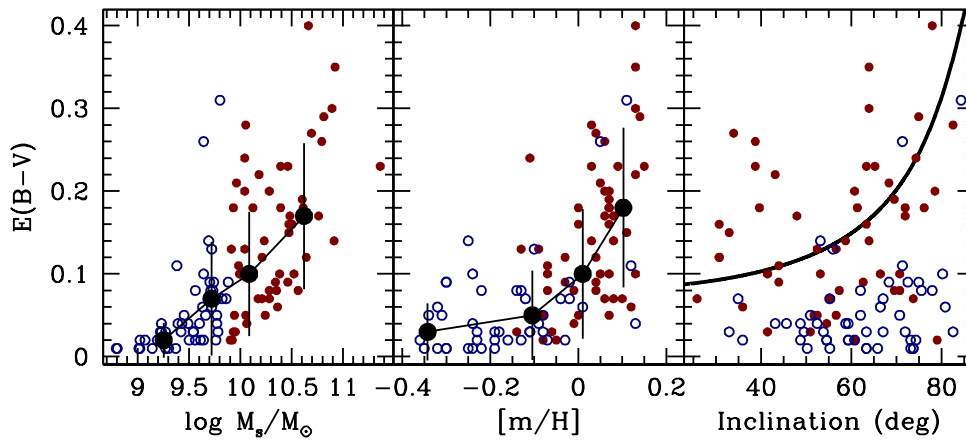
**Figure 10.** Model constraints on the colour excess, with respect to stellar mass, metallicity or inclination. The red solid (blue open) dots correspond to stellar masses $\log M_s/M_\odot > 10$ ($< 10$). The big solid dots with error bars in the left and middle panels give the median and RMS scatter of the complete sample, binned at fixed number of galaxies per bin. The rightmost panel includes a prescription from Tully & Fouqué (1985), with $f = 0.2$ and $\tau = 0.5$ (solid line).

massive disc subsample, whereas lower mass discs are not affected so strongly with respect to disc inclination.

### 4.4 Star formation rates (SFRs)

Ongoing star formation rates can be derived from emission line luminosities. In this paper, we use SFRs from [O II], using the conversion from Kennicutt (1992). Fig. 11 presents the SFRs (*top*) and specific SFRs (SSFR, defined as the SFR per unit stellar mass, *bottom*) with respect to either stellar mass (*left*) or average age (*right*). The sample is split with respect to redshift at the median value of the subsample comprising 65 galaxies where SFRs could be determined ($z_M = 0.60$), with solid (open) circles corresponding to low (high) redshift. Only a subset of the full sample is presented here because the derivation of SFRs require estimates of [O II] luminosities. Characteristic error bars, at the $1\sigma$ level are shown for reference. A strong correlation is found between SSFR and age. In the bottom-left panel, the rates measured in our sample are compared with the general trend of star-forming galaxies from Brinchmann & Ellis (2000) at $z \sim 0.6$ (solid line) and $z \sim 0.9$ (dashed line).

## 5 CONCLUSIONS

By comparing optical to NIR photometry of a sample of disc galaxies at intermediate redshift, with a simple set of phenomenological one-zone models including chemical enrichment, we are able to explore the formation of these systems and the evolution of the Tully-Fisher relation. We find a strong correlation between the parameters that describe the star formation history and stellar mass. The formation epoch and star formation (SF) timescale ($\tau_1$) are especially correlated with stellar mass, showing the usual downsizing trend, with the most massive discs forming around $z \sim 3$, with SF timescale $\tau_1 \sim 4$ Gyr. The enrichment timescale ($\tau_2$) decreases with increasing mass, reflecting a very efficient process for the build-up of metallicity in the most massive galaxies ($\tau_2 \lesssim 1$ Gyr). These are the typical timescales for the enrichment of massive early-type galaxies

(see, e.g. Ferreras & Silk 2001), however, our massive discs have longer SF timescales, resulting in an extended distribution of stellar ages. On the Tully-Fisher plane, age does not introduce a segregation at fixed circular speed, suggesting mild evolution of the Tully-Fisher relation with redshift.

We also present the model fits with respect to dynamical mass (measured within three scale lengths) and find a similar trend as with respect to stellar mass. However, the ratio of the two – an estimator of dark matter fraction, or feedback efficiency – seem not to correlate so strongly with the model parameters, reinforcing the idea that mass is the strongest, first order driver of the star formation histories of galaxies. Nevertheless, on the Tully-Fisher diagram (Fig. 9), at fixed $M_s/M_{\rm dyn}$, older galaxies have faster circular speeds, perhaps reflecting the fact that older discs would have formed in higher density halos, hence the higher $V_{\rm MAX}$. The difference is rather small, and a more detailed analysis – based on spectroscopic data with high SNR and accurate flux calibration – is needed to confirm this trend.

Our model includes dust as a free parameter, treated as a simple dust screen. Our findings agree independently with the formalism of Tully & Fouqué (1985) for the most massive discs (stellar mass $\gtrsim 10^{10} M_\odot$), with lower mass discs featuring no significant trend between colour excess and inclination.
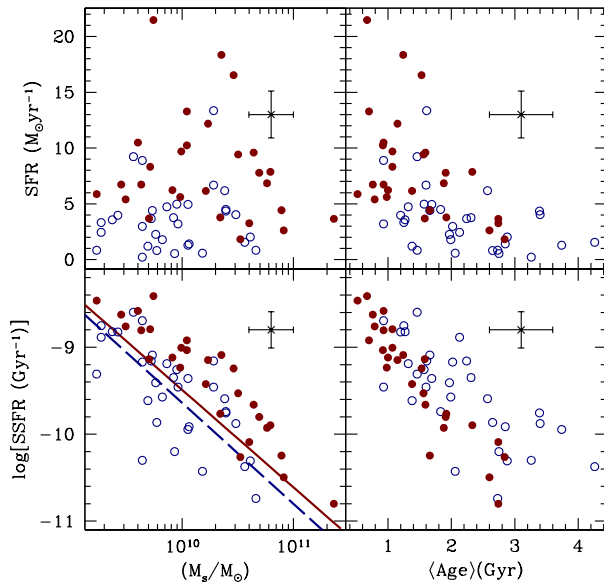
### REFERENCES

Bell, E. F., de Jong, R. S., 2001, ApJ, 550, 212
Brinchmann, J., Ellis, R. S., 2000, ApJ, 536, L77
Bruzual, G., 1983, ApJ, 273, 105

**Figure 11.** Correlation of star formation rate (SFR, *top*) and specific star formation rate (SSFR, *bottom*) with respect to stellar mass (*left*) or average age of the stellar populations (*right*). The data are split at the median redshift of the subsample where SFR information is available (red solid dots: $z > 0.60$). The blue dashed and red solid lines correspond to the "main sequence" of star forming galaxies at $z \sim 0.6$ and $z \sim 0.9$, respectively (Brinchmann & Ellis 2000).

Bruzual, G., Charlot, S., 2003, MNRAS, 344, 1000

Böhm, A., et al. 2004, A&A, 420, 97

Böhm, A., Ziegler, B., 2007, ApJ, 668, 846

Cardelli, J. A., Clayton, G. C., Mathis, J. S., 1989, ApJ, 345, 245

Cimatti, A., Daddi, E. & Renzini, A., 2006, A&A, 453, L29

Cowie, L. L., Songaila, A., Hu, E. M., Cohen, J. G., 1996, AJ, 112, 839

de La Rosa, I. G., La Barbera, F., Ferreras, I., de Carvalho, R. R. 2011, MNRAS, 418 L74

Dutton, A. A., van den Bosch, F. C., Dekel, A., Courteau, S., 2007, ApJ, 654, 27

Fernández-Lorenzo, M., Cepa, J., Bongiovanni, A., Castañeda, H., Pérez García, A. M., Lara-López, M. A., Pović, M., Sánchez-Portal, M., 2009, A&A, 496, 389

Ferreras, I. & Silk, J., 2001, ApJ, 557, 165

Ferreras, I., Silk, J., Böhm, A. & Ziegler, B., 2004, MNRAS, 355, 64

Flores, H., Hammer, F., Puech, M., Amram, P., Balkowski, C., 2006, A&A, 455, 107

Gallazzi, A., Charlot, S., Brinchmann, J,. White, S. D. M., Tremonti, C. A., 2005, MNRAS, 362, 41

Giovanelli, R., Haynes, M. P., da Costa, L. N., Freudling, W., Salzer, J. J., Wegner, G., 1997, ApJ, 477, L1

Governato, F. et al., 2009, MNRAS, 398, 312

Heidt, J., et al. 2003, A&A, 398, 49

Kauffmann, G., et al., 2003, MNRAS, 341, 54

Kennicutt, R. C., 1992, ApJ, 388, 310

Khalatyan, A., Cattaneo, A., Schramm, M., Gottlöber, S., Steinmetz, M., Wisotzki, L., 2008, MRAS, 387, 13

Kodama, T., et al., MNRAS, 350, 1005

McGaugh, S. S., Schombert, J. M., Bothun, G. D., de Blok,

W. J. G., 2000, ApJ, 533, L99

McGaugh, S. S., 2012, AJ, 143, 40

Mathis, H., Lemson, G., Springel, V., Kauffmann, G., White, S. D. M., Eldar, A., Dekel, A., 2002, MNRAS, 333., 739

Metcalfe, N., Shanks, T., Campos, A., McCracken, H. J., Fong, R., 2001, MNRAS, 323, 795

Miller, S. H., Bundy, K., Sullivan, M., Ellis, R. S., Treu, T., 2011, ApJ, 741, 115

Miller, S. H., Ellis, R. S., Sullivan, M., Bundy, K., Newman, A. B., Treu, T., 2012, ApJ, 753, 74

Moster B. P., Somerville R. S., Maulbetsch C., van den Bosch F. C., Macciò A. V., Naab T., Oser L., 2010, ApJ, 710, 903

Pagel, B. E. J., 1997, Nucleosynthesis and Chemical Evolution of Galaxies. Cambridge University Press, Cambridge

Peng, C. Y., Ho, L. C., Impey, C. D., Rix, H.-W., 2002, AJ, 124, 266

Pérez-González, P. G., et al., 2008, ApJ, 675, 234

Portinari, L., Sommer-Larsen, J., 2007, MNRAS¡ 375, 913

Puech, M. et al., 2008, A&A, 484, 173

Rogers, B., Ferreras, I., Pasquali, A., Bernardi, M., Lahav, O., Kaviraj, S., 2010, MNRAS, 405, 329

Schlegel, D. J., Finkbeiner, D. P., Davis, M., 1998, ApJ, 500, 525

Tonini, C., Maraston, C., Ziegler, B., Böhm, A., Thomas, D., Devriendt, J., Silk, J., 2011, MNRAS, 415, 811

Tully, R. B., Fisher, J. R., 1977, A&A, 54, 661

Tully, B. & Fouqué, 1985, ApJS, 58, 67

Tully, R. B., Pierce, M. J., Huang, J.-S., Saunders, W., Verheijen, M. A. W., Witchalls, P. L., 1998, AJ, 115, 2264

van den Bosch, F. C., et al. 2008, MNRAS, 387, 79

Vogt, N. P., Forbes, D. A., Phillips, A. C., Gronwall, C., Faber, S. M., Illingworth, G. D., Koo, D. C. 1996, ApJ, 465, L15

Weiner, B., et al. 2006, ApJ, 653, 1049

Ziegler, B. L., et al. 2002, ApJ, 564, L69